Solar UV index and UV dose determination with photochromic hackmanites: From the assessment of the fundamental properties to the device.

Isabella Norrbo[1,2], Antton Curutchet[3], Ari Kuusisto[4], Jaakko Mäkelä[2,5], Pekka Laukkanen[5], Petriina Paturi[5], Tero Laihinen[1], Jari Sinkkonen[1], Erik Wetterskog[6], Fikret Mamedov[7], Tangui Le Bahers[3], Mika Lastusaari[1,8]

[1]University of Turku, Department of Chemistry, FI-20014, Turku, Finland.
[2]University of Turku Graduate School (UTUGS), Doctoral Programme in Physical and Chemical Sciences (PCS), FI-20014 Turku, Finland
[3]University of Lyon, ENS de Lyon, CNRS, Université Claude Bernard Lyon 1, Laboratoire de Chimie UMR 5182, F-69342 Lyon, France.
[4]Solar Simulator Finland Ltd, FI-20660 Littoinen, Finland.
[5]University of Turku, Department of Physics and Astronomy, FI-20014 Turku, Finland.
[6]Uppsala University, Department of Engineering Sciences, SE-75120 Uppsala, Sweden.
[7]Uppsala University, Department of Chemistry, SE-75120 Uppsala, Sweden.
[8]Turku University Centre for Materials and Surfaces (MatSurf), FI-20014 Turku, Finland.

Supporting Information

Contents

I. Experimental section

Synthesis of $(Na_{1-x}M_x)_8Al_6Si_6O_{24}(Cl,S)_2$ (M = K or Rb). The hackmanite samples were prepared with a solid-state reaction using stoichiometric amounts of Zeolite A (Sigma-Aldrich, product no. 96096), NaCl (J. T. Barker, 99.5%), and Na2SO4 (E. Merck, 99%) as starting materials. The materials were prepared with the S/Cl molar ratios of 0.06 because this ratio leads to the maximum photochromic response. The Rb and K doping were obtained by replacing 25% of the NaCl by KCl (E. Merck, Suprapur) or RbCl (E. Merck, Suprapur), thus leading to a doping fraction (noted x) of nominally 25%. Zeolite A was first dried at 500 °C for 1 h. The initial mixture was then heated at 850 °C in air for 48 h. The product was freely cooled to room temperature and ground. Finally, the product was reheated at 850 °C for 2 h under a flowing 12% H_2 + 88% N2 atmosphere. The as-prepared materials were washed with water to remove any excess MCl (M = Na, K, Rb) impurities.

Characterization. The purity of the materials was checked with routine X-ray powder diffraction measurements using a Huber G670 detector with Cu Kα1 radiation (λ = 1.54060 Å). The unit cells were refined from the X-ray diffraction data using the Rietveld method.[1] with the program FullProf [2].

The tenebrescence excitation spectra were compiled as follows: The white sample was partly irradiated within a Varian Cary Eclipse spectrometer (Xe lamp) for 1 min with the chosen wavelength. Then the sample was photographed and the RGB values for the irradiated and non-irradiated parts were determined using the ImageJ program.[3] The non-irradiated:irradiated RGB ratio was then used as the color intensity at each irradiation wavelength.

The composition distribution of the materials was investigated with SEM-EDS. One hundred randomly chosen grains were included per sample and the results were statistically evaluated using the IBM SPSS 23 program.[4] The setup was a Leo 1530 Gemini microscope equipped with a Thermo Scientific UltraDry SDD EDS-system.

Tenebrescence rise and fade curves were recorded with the reflectance mode of an Avantes Avaspec HS-TEC CCD spectrometer. The UVC source was a hand-held UV lamp (UVP UVGL-25, 4 W) operating at 254 nm. The irradiances were determined with an Opsytec Dr. Gröbel Radiometer RM 12 equipped with a RM12 sensor calibrated for UVC. The irradiance level was controlled by adjusting the distance between the lamp and the hackmanite material. An Avantes AvaSpec-2084x14 spectrometer was used in reflectance mode to record the steady state reflectance spectra. In both setups, the sample was illuminated at 2700 lx (as measured with a with Hagner E4-X luxmeter) with an incandescent light bulb.

The valence of sulfur was studied with X-ray photoelectron spectroscopy (XPS) measurements carried out using a Perkin-Elmer PHI 5400 spectrometer with a MgKα X-ray source and a hemispherical electron energy analyzer. A neutralizer with a constant electron flux was used during the measurements to avoid electrical charging of the insulating powder samples. The fitting was carried out using CasaXPS software Version 2.3.16.[5] Measurements were made before and after irradiating the sample at 254 nm with a hand-held UV lamp (UVP UVGL-25, 4 W).

The 35Cl solid state nuclear magnetic resonance (NMR) spectra were recorded at room temperature with a Bruker AV400 apparatus using 10 000 Hz spinning and a 0.1 s relaxation time. The ppm scale was calibrated against 1 molar aqueous NaCl, whose resonance was assigned to 0.0 ppm.

The electron paramagnetic resonance (EPR) spectra were measured using a Bruker ELEXSYS E500 X band EPR spectrometer equipped with a SuperX EPR049 microwave bridge and a SHQ4122 resonator at a frequency of 9.28 GHz. The measurements at 15 K were performed using an Oxford instruments cryostat and an ITC-4 temperature controller. A microwave power of 5 mW and a modulation amplitude of 3 G were used. A spectrum was first measured for a fully colored sample. The sample was then heated for 20 min at 200°C to remove the color. The resulting material was used for the measurement of a white sample. The EPR spectra were analyzed with Xepr Bruker software.

Magnetization versus temperature measurements were carried out using a MPMS XL SQUID magnetometer. A magnetic field of 50 mT (40 kA/m, 500 Oe) was applied while measuring the magnetization from 2 - 300 K. The samples were mounted in a polymeric sample holder, and the diamagnetic background of the sample holder was subtracted.

For the UVI-dependent coloration measurements a LOT/QD LS0500 solar simulator lamp was used as the irradiation source. The UVI value obtained from the lamp was measured with a Solarmeter 6.5 UV Index radiometer and controlled with the distance between the lamp and the hackmanite sample. For UVC coloration, the irradiation setup was the same as that described for tenebrescence rise above. For UVI and UVC, 10 s irradiation times were used. The color intensity after UVI, UVC and X-ray exposure was determined from reflectance spectra or photographs as described above.

Computational details. All calculations were performed using the Density Functional Theory (DFT) framework with the global hybrid functional PBE0[6] in periodic boundary condition (PBC) along with the ab initio CRYSTAL14 code[7,8], using localized (gaussian) basis sets and solving self-consistently the Hartree-Fock and Kohn-Sham equations thus allowing the efficient use of hybrid functionals. For the Na, Si, Cl, Al, O, Li and K atoms the all-electron double-zeta basis sets with polarization functions 85-11G(d), 88-31G(d), 66-31G(d), 86-21G(d), 66-31G(d), 5-11G(d) and 865-11G(d) were used respectively. For the S atom, that is directly involved in the spectroscopic properties of the system, the triple-zeta basis set 86-311G(2d) was used. For the Rb atoms, the Hay-Watt small core pseudopotential was used along with the 31G(d) basis for the 9 valence electrons. To describe the trapped electron, a basis with the 11G(d) structure was optimized for each system (coefficients of these basis are given in section V below). Due to the large size of the system (2x2x2 supercell of the primitive sodalite unit cell), the reciprocal space was sampled with a single k-point (the Γ point) for the geometry optimizations while the density of states (DOS) were obtained using a 4x4x4 k-points mesh. The convergence criterion for the SCF cycle was fixed at 10^{-7} Ha per unit cell.

II. Correspondence between orbitals occupancy and electronic state

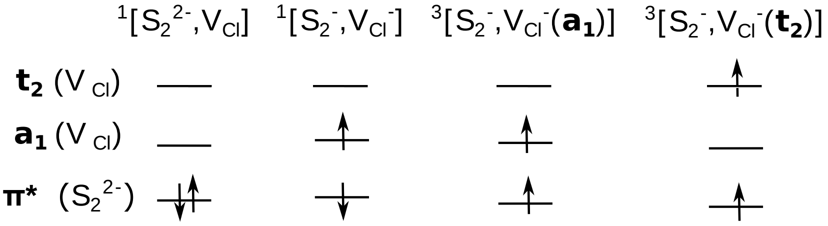

Figure S1. Orbital description of the electronic states.

III. X-ray diffraction

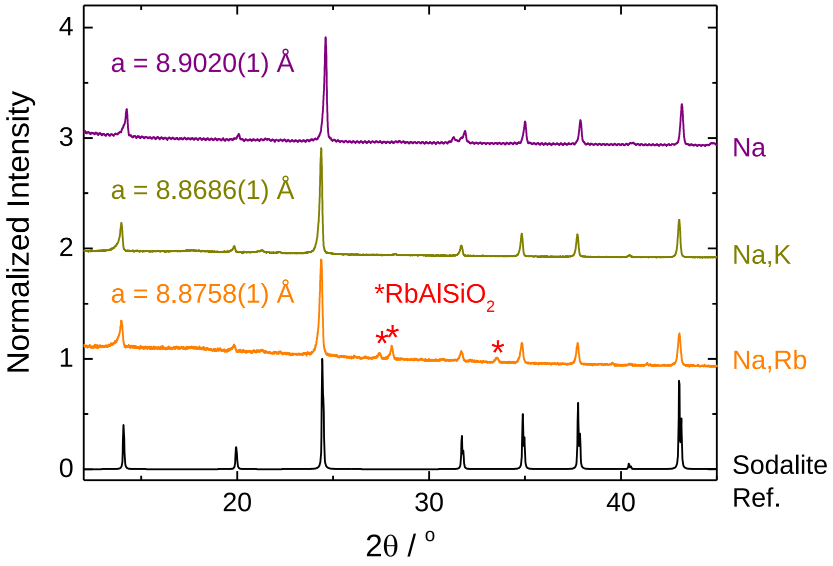

Figure S2. X-ray powder diffraction patterns of all studied hackmanite materials. The refined unit cell parameters are given, as well.

IV. Distribution of compositions

The inter-grain distribution of x in $(Na_{1-x}M_x)_8Al_6Si_6O_{24}(Cl,S)_2$, where M = K or Rb was determined based on the observed Na, K and Rb contents, *i.e.* w(Na), w(K) and w(Rb), as follows:

x(K) = w(K) / [w(K)+w(Na)] and

x(Rb) = w(Rb) / [w(Rb)+w(Na)]

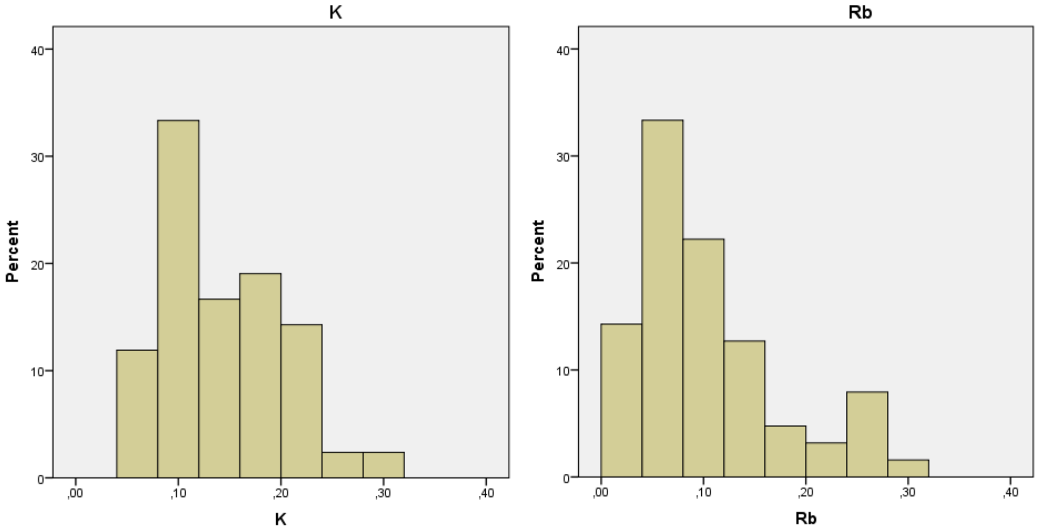

Figure S3. Composition distribution of K (left) and Rb (right) in the respective hackmanites. The value on the x axis corresponds to x in $(Na_{1-x}M_x)_8Al_6Si_6O_{24}(Cl,S)_2$, where M = K or Rb.

Table S1. Statistics of the composition distribution and the M:Cl ratio.

	K	K:Cl	Rb	Rb:Cl
Mean	.1374	.4010	.0973	.3306
Median	.1300	.3900	.0800	.3100
Std. Deviation	.0605	.1115	.0719	.2173
Variance	.004	.012	.005	.047

V. DFT simulation

In the present calculations, 6.25 % of the chloride ions were considered to be replaced by S_2^{2-} and 6.25 % of the chloride sites were considered to be empty (i.e. vacancies). Furthermore, 0.0, 1.6, 3.2 or 4.8 % of the Na^+ sites was considered to be doped by Li^+, K^+ or Rb^+. These percentages correspond to no, one, two or three Na^+ ions substituted in the vicinity of the chloride vacancy.

A 2x2x2 supercell was considered with the center chlorine removed giving a vacancy, noted V_{Cl}. For the S_2^{2-} species, the most stable site with respect to the vacancy position was chosen based on earlier results[9]. This corresponds to a doping fraction of 6.25 % (in chlorine content). To simulate the K, Li and Rb doping, the most stable Na^+ site for the substitution was determined by replacing one Na^+ by one of the dopant (Li^+, K^+ or Rb^+) in the supercell, leading to a doping concentration of 1.6 % (in Na content). Four different locations (see Figure 2 in the main text) were tested for the alkali metal dopant to probe the effect of the distance between the dopant and the S_2^{2-} as well as the V_{Cl}. Briefly, the a site corresponds to the tetrahedron surrounding the S_2^{2-} but not in contact with V_{Cl}. The b site is the position both in contact with S_2^{2-} and V_{Cl}. The c position is the one surrounding V_{Cl} while the d position is neither close to S_2^{2-} nor to the vacancy. The Table S2 summarizes the relative stability of these substitutions. It clearly appears that for all systems, the most stable position for the doping corresponds to the tetrahedron surrounding the vacancy (b and c positions). The reason of these preferred positions is probably the larger flexibility of the tetrahedron surrounding the vacancy that is able to accommodate the local geometrical distortion induced by the doping. Taking into account the multiplicity of each site in the system (given in Table S2), we can estimate the Boltzmann distribution of the dopant on each site. The conclusion is that for Li and Rb dopant, the tetrahedron surrounding the vacancy has the largest probability to be doped compared to the other tetrahedrons. For K, while the doping in the tetrahedron surrounding V_{Cl} is more stable, the close energy for the doping on the other tetrahedra leads to a distribution of K lower around the vacancy (16%).

Table S2. Relative energy for the Na substitution by Li, K and Rb as a function of the site (cf Figure S5) along with the distribution taking into account both the relative energy and the multiplicity of each site.

	Site	Multiplicity	Energy / eV	Distribution / %
Li	a	4	0.21	0
	b	**1**	**0.00**	95
	c	3	0.11	**5**
	d	56	0.36	0
K	a	4	0.29	0
	b	1	0.31	0
	c	**3**	**0.00**	**16**
	d	56	0.03	84
Rb	a	4	0.62	0
	b	1	0.47	0
	c	**3**	**0.00**	**100**
	d	56	0.22	0

V.1- PBE0 benchmarck for bandgaps.

Table S3. Experimental and computed bandgaps (in eV) of insulators along with the relative error in brackets.

	SiO_2 α-quartz	**NaCl**	**Al_2O_3** Corundum
Exp	11.5	8.5	8.8
PBE0	10.93 (-5.0%)	8.85 (+4.1%)	9.11 (+3.5%)

V.2- Vacancy basis set.

Table S4. Optimized coefficients for the 11G(d) basis set of the vacancy for the Li doping. The letters in index correspond to the positions where Na was substituted by Li. The ø system corresponds to the undoped hackmanite.

	ø	$\mathbf{Li_a}$	$\mathbf{Li_b}$	$\mathbf{Li_c}$	$\mathbf{Li_d}$	$\mathbf{Li_{bc}}$	$\mathbf{Li_{bcc}}$
SP	0.176	0.200	0.081	0.135	0.181	0.085	0.082
SP	0.036	0.037	0.037	0.035	0.037	0.035	0.035
D	0.051	0.052	0.050	0.051	0.054	0.060	0.049

Table S5. Optimized coefficients for the 11G(d) basis set of the vacancy for the K doping. The letters in index correspond to the positions where Na was substituted by K.

	$\mathbf{K_a}$	$\mathbf{K_b}$	$\mathbf{K_c}$	$\mathbf{K_d}$	$\mathbf{K_{cc}}$	$\mathbf{K_{ccc}}$
SP	0.081	0.224	0.062	0.189	0.057	0.062
SP	0.037	0.040	0.034	0.037	0.034	0.034
D	0.050	0.052	0.054	0.054	0.055	0.059

Table S6. Optimized coefficients for the 11G(d) basis set of the vacancy for the Rb doping. The letters in index correspond to the positions where Na was substituted by Rb.

	$\mathbf{Rb_a}$	$\mathbf{Rb_b}$	$\mathbf{Rb_c}$	$\mathbf{Rb_d}$	$\mathbf{Rb_{cc}}$	$\mathbf{Rb_{ccc}}$
SP	0.199	0.044	0.045	0.168	0.052	0.060
SP	0.038	0.032	0.033	0.036	0.032	0.033
D	0.050	0.054	0.049	0.051	0.060	0.061

V.3- Density of states.

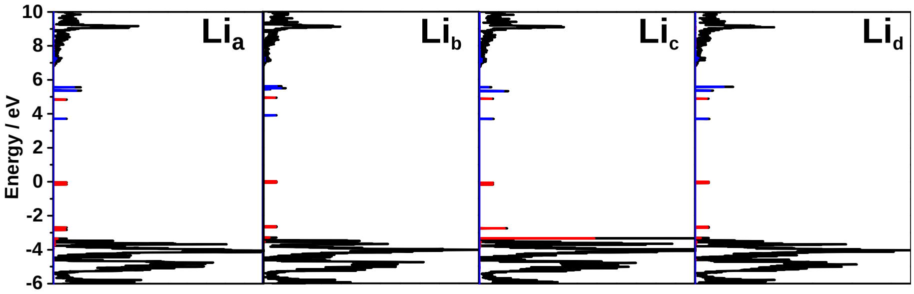

Figure S4. Density of states for one Na substituted by one Li. Black, red and blue curves correspond to the total DOS, the DOS project on S_2^{2-} and the DOS projected on V_{Cl} respectively. The letter in subscript indicates the position of doping (cf main manuscript).

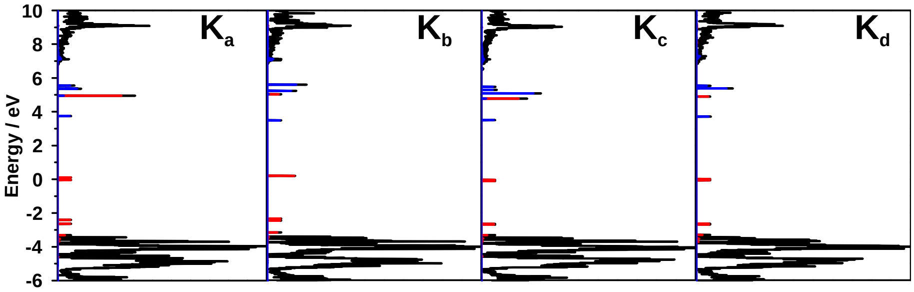

Figure S5. Density of states for one Na substituted by one K. Black, red and blue curves correspond to the total DOS, the DOS project on S_2^{2-} and the DOS projected on V_{Cl} respectively. The letter in subscript indicates the position of doping (cf main manuscript).

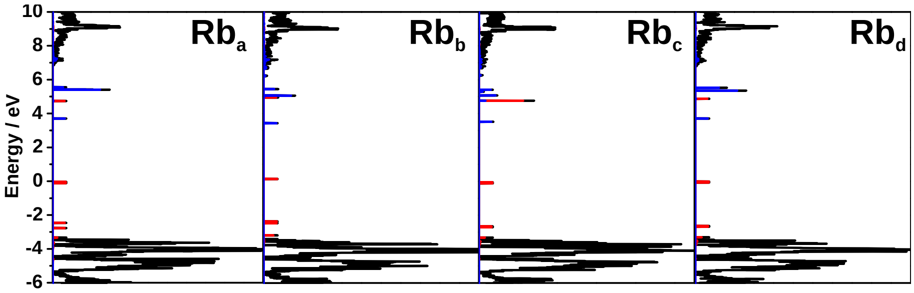

Figure S6. Density of states for one Na substituted by one Rb. Black, red and blue curves correspond to the total DOS, the DOS project on S_2^{2-} and the DOS projected on V_{Cl} respectively. The letter in subscript indicates the position of doping (cf main manuscript).

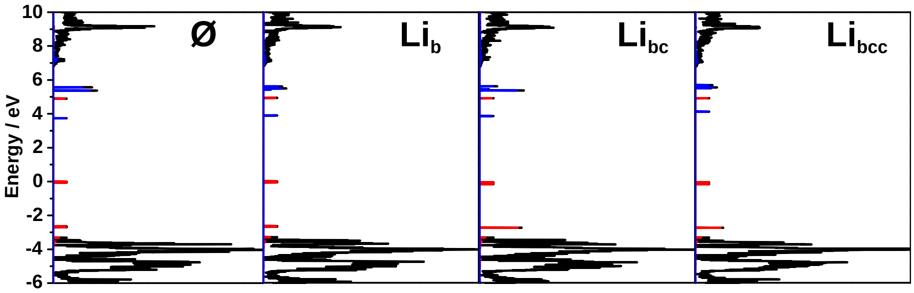

Figure S7. Density of states for successive Na substitution by one Li around V_{Cl}. Black, red and blue curves correspond to the total DOS, the DOS project on S_2^{2-} and the DOS projected on V_{Cl} respectively. The letter and their number in subscript indicate the doping positions (cf main manuscript) and the number of Na substituted.

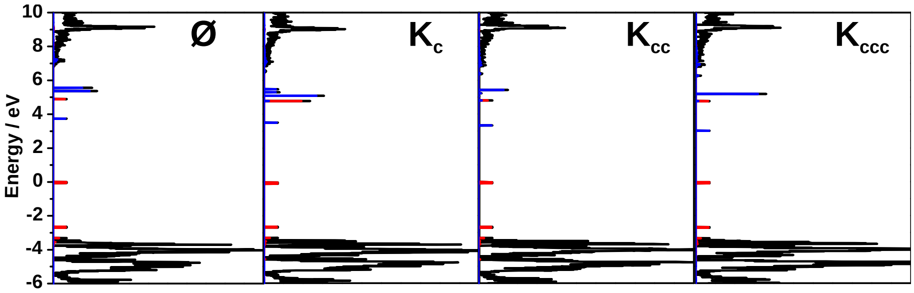

Figure S8. Density of states for successive Na substitution by one K around V_{Cl}. Black, red and blue curves correspond to the total DOS, the DOS project on S_2^{2-} and the DOS projected on V_{Cl} respectively. The letter and their number in subscript indicate the doping positions (cf main manuscript) and the number of Na substituted.

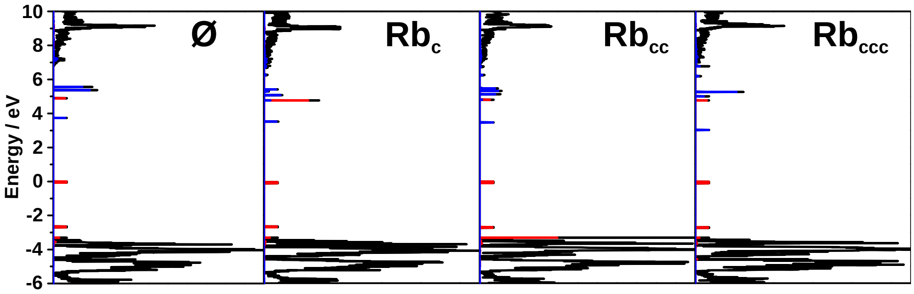

Figure S9. Density of states for successive Na substitution by one Rb around V_{Cl}. Black, red and blue curves correspond to the total DOS, the DOS project on S_2^{2-} and the DOS projected on V_{Cl} respectively. The letter and their number in subscript indicate the doping positions (cf main manuscript) and the number of Na substituted.

V.4- Energy gaps for coloration mechanism 1

The energy gap between the last occupied orbital, $\pi^*(S_2^{2-})$, and the conduction band of the undoped hackmanite is 6.81 eV.

Table S7. Energy gap between $\pi^*(S_2^{2-})$ and the bottom of conduction band (in eV) for the different substitution site.

Position	Li	K	Rb
a	6.84	6.67	6.87
b	6.82	6.60	6.02
c	6.79	6.51	6.26
d	6.80	6.81	6.79

Table S8. Energy gap between $\pi^*(S_2^{2-})$ and the bottom of conduction band (in eV) by increasing the number of dopant around the vacancy from 0 (undoped system) to three Na substituted.

Number of dopant around V_{Cl}	Li	K	Rb
0	6.81	6.81	6.81
1	6.82	6.51	6.26
2	6.83	6.35	6.23
3	6.84	6.26	6.19

V.5- Energy gaps for coloration mechanism 2

The energy gap between the last occupied orbital, $\pi^*(S_2^{2-})$, and the first unoccupied orbital, $a_1(V_{Cl})$, band of the undoped hackmanite is 3.74 eV.

Table S9. Energy gap between $\pi^*(S_2^{2-})$ and $a_1(V_{Cl})$ (in eV) for the different substitution site.

Position	Li	K	Rb
a	3.75	3.64	3.74
b	3.77	3.29	3.28
c	3.89	3.54	3.57
d	3.71	3.70	3.72

Table S10. Energy gap between $\pi^*(S_2^{2-})$ and $a_1(V_{Cl})$ (in eV) by increasing the number of dopant around the vacancy from 0 (undoped system) to three Na substituted.

Number of dopant around V_{Cl}	Li	K	Rb
0	3.74	3.74	3.74
1	3.77	3.54	3.57
2	3.92	3.35	3.49
3	4.18	3.04	3.06

V.6- Discussion on the coloration mechanism

For the mechanism (1), while the substitution of Na by K and Rb reduces the energy gap between the CB and $\pi^*(S_2^{2-})$, as observed experimentally, this energy remains higher than 6 eV and even around 7 eV for the pure hackmanite. A benchmark of PBE0 functional on the bandgap simulation performed on wide bandgap semiconductors indicates that the standard deviation of this functional on wide bandgap energies is 5%. Consequently, the computed energies necessary to perform the mechanism (1) are by far larger than the experimental threshold (lower than 4.2 eV). On the other hand, the energy gap of the mechanism (2) is computed around 3.7 eV for the pure hackmanite, thus very close to the experimental value of 4.2 eV. A recent investigation performed by some of us on the simulation of the direct charge transfer between S_2^{2-} and V_{Cl} (mechanism (2) in this work) showed that the simulation of the energy of this transfer is better reproduced by the computationally very expensive post-Hartree-Fock methods (SAC-CI). In the present work, we decided to stay at the DFT level, this is perfectly reliable to understand the trends observed experimentally upon doping. The Figure 1d in the main paper presents the evolution of this gap upon Li, K and Rb doping around the vacancy. There is a clear opposite behaviour between Li doping on one side, inducing an increase of the energy threshold, and K and Rb doping inducing a decrease of this energy. The K and Rb doping placed around the vacancy have almost the same influence on the absorption threshold contrary to experiment where Rb leads to a more marked energy lowering of the F-center generation threshold. The results obtained here helps to understand this observation. At a given K and Rb concentration, all the Rb atoms are placed around V_{Cl} because this is the most stable doping site (Table S2) while K atoms can be placed on d and c positions thus not necessarily around the vacancy. Only the K atoms placed on c position have an influence on the absorption threshold. This leads to a lower effect compared to Rb because a large fraction of K dopants is placed on the inactive d positions.

VI. EPR measurements

EPR measurements clearly confirmed the presence of S_2^- radicals, as well as the increase of their concentration upon coloration, with the signals at g = 2.005 and 2.032 (Figure S10).[10] The color center signal in hackmanites has been reported as a 13-line structure centered at g = 2.002 with a 30.6 G spacing.[11] In the present case, the center line is not very clear because of the strong signal of S_2^-. However, it is possible that a very weak 13-line structure is present (Figure S10). In addition to these, the EPR spectrum also shows a weak signal of Ti^{3+} (g = 1.987) which is present as a ppm level impurity in these materials[12].

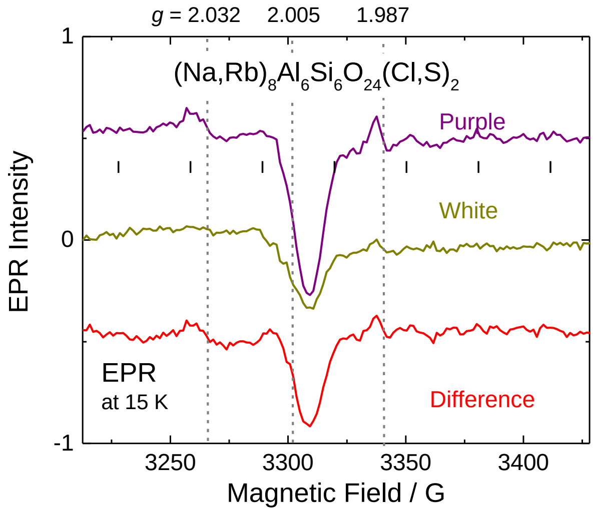

Figure S10. EPR spectra for a white and colored $(Na,Rb)_8Al_6Si_6O_{24}(Cl,S)_2$ material at 15 K. The short vertical black lines are drawn with a 30.6 G spacing to indicate a possible multiline structure.

VII. Solid state ^{35}Cl MAS-NMR measurements

Trill et al.[13] have shown that the ppm values of the NMR signals of $Na_8Al_6Si_6O_{24}Cl_2$ are dependent on the concentration of color centers in the material. For example the ^{35}Cl MAS-NMR signal of a species without any nearby color centers shifts from -124 to -120 ppm with color center concentrations from 17 to 84 % (with respect to the number of Cl sites). In our case, the nominal concentration is 5 %, which would suggest a value of ca. -125 ppm if extrapolated from the data of Trill et al.[13]. However, our results show signals at ca. -130 ppm (Figure S11) indicating a lower concentration. Also, there are no significant differences between the white and colored samples.

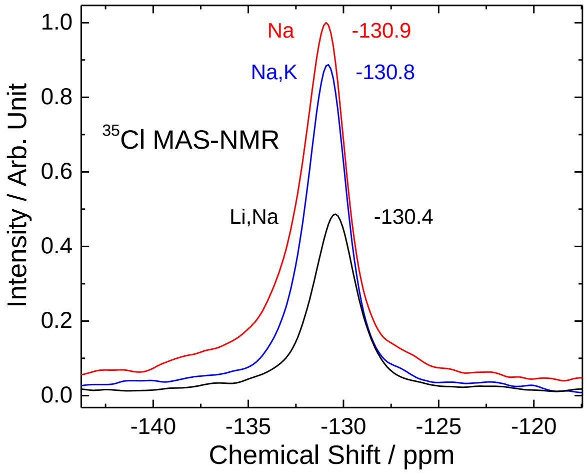

Figure S11. Solid state ^{35}Cl MAS-NMR spectra of samples with different alkali metal compositions.

VIII. Magnetization measurements

We calculated the difference between the signals of the white and the fully colored material. The resulting curve is a more or less horizontal line thus suggesting that the color center shows a temperature-independent behavior, i.e. van Vleck paramagnetism[14]. This is due to the fact that the lowest $^3[S_2^{-},V_{Cl}^{-}(\mathbf{a_1})]$ triplet is a non-magnetic $^3P_0$ state with $^3P_1$ and $^3P_2$ nearby in energy. Then, taking into account the difference in magnetization between the colored and white forms ($2.0\cdot10^{-4}$ Am^2kg^{-1}, Figure S12) as well as the magnetic moment of $^3P_1$ (2.1 Bohr magnetons), we can estimate the color center coordination to be 10^{19} kg^{-1}. This corresponds to ca. 0.1 % of color centers with respect to Cl sites. Being an allowed $A_1 \rightarrow T_2$ transition[9] (with an oscillator strength of around 0.3 a.u.), the absorption of the color center will show a strong color even if the F-center concentration is not very high.

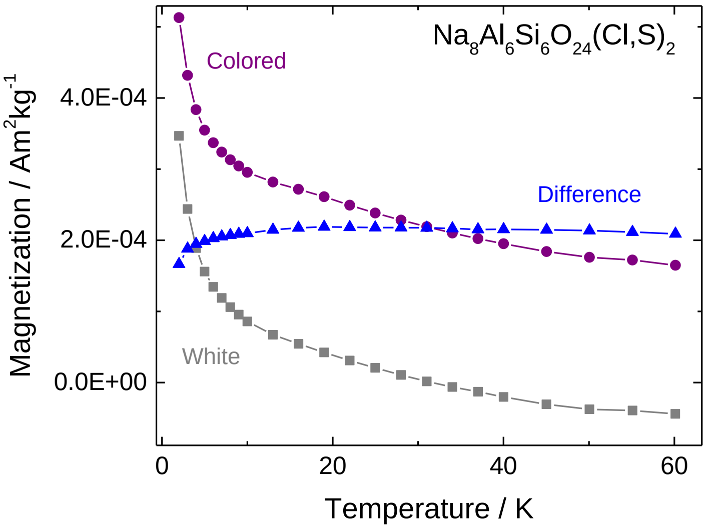

Figure S12. Magnetization curves for a white and colored $Na_8Al_6Si_6O_{24}(Cl,S)_2$ material.

IX. Reflectance Measurements

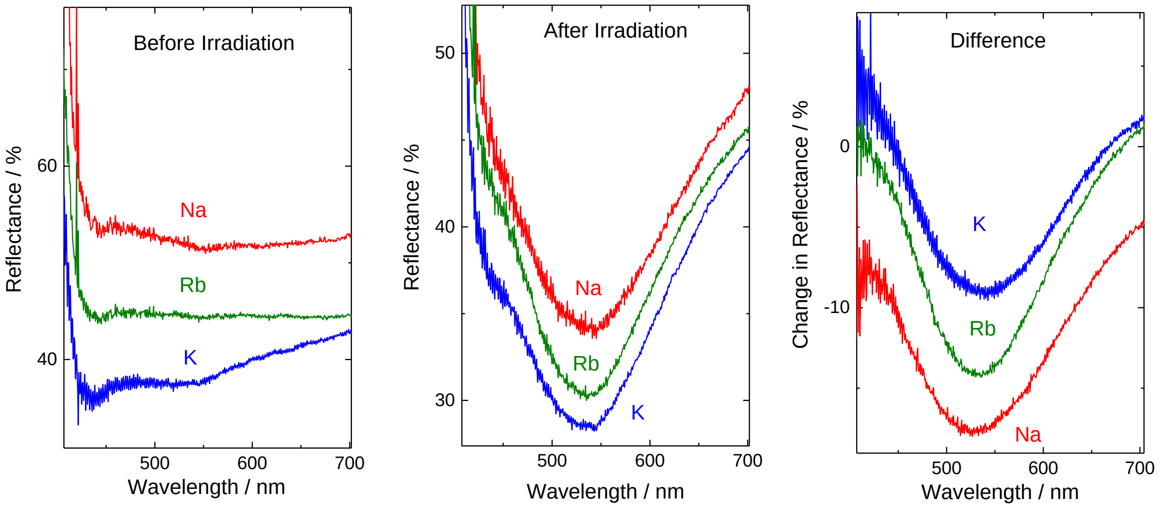

Figure S13. Reflectance measurements of all studied hackmanite materials: before and after irradiation as well as the difference between before and after.

X. Initial rise fitting of thermotenebrescence curves

The ln(color intensity) vs. reciprocal temperature (in K^{-1}) curves were fitted with a linear equation. According to the initial rise method[15], the activation energy is obtained from the slope which is equal to $-E_T/k$ (k = Boltzmann constant).

Table S11. Results of initial rise fittings of the thermotenebrescence curves.

	Na		K		Rb	
	Value	Standard Error	Value	Standard Error	Value	Standard Error
Intercept	19.12328	0.51987	15.06835	0.43356	13.3452	0.14057
Slope	-5536.88	227.9765	-3281.57	164.8773	-2722.26	63.26323
Residual Sum of Squares	9.48521		11.04928		1.82617	
Pearson's r	-0.92738		-0.87777		-0.96689	
Adj. R-Square	0.85857		0.76854		0.93436	

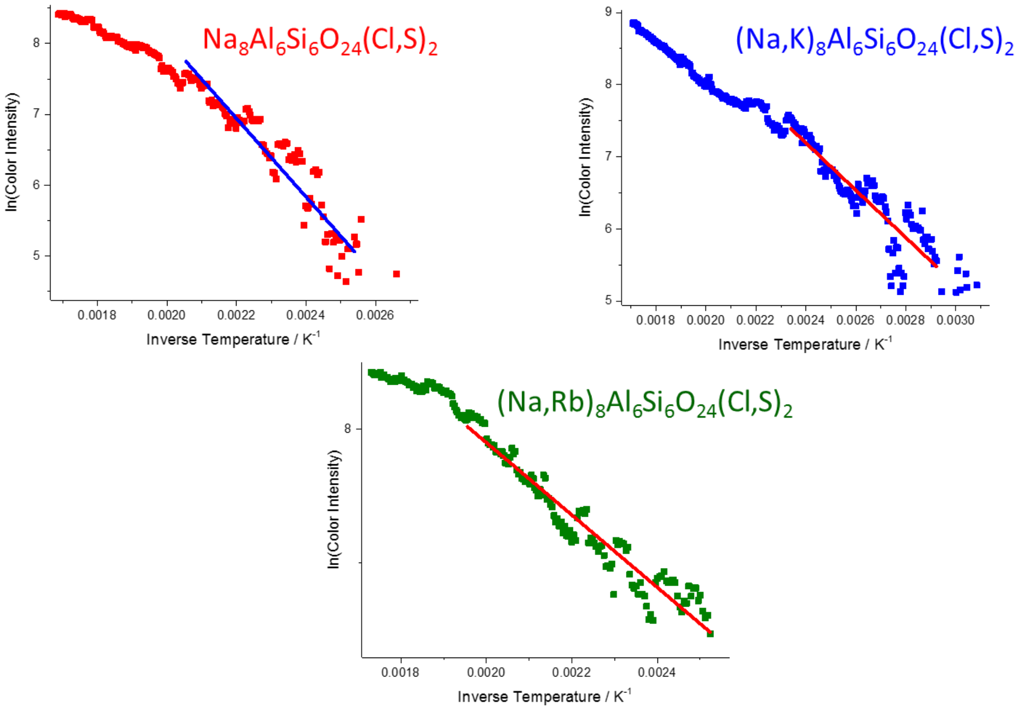

Figure S14. Initial rise fittings of the thermotenebrescence curves.

XI. Fitting of tenebrescence fading curves

The fading curves were fit to a two-term exponential decay function:

color intensity = A1*exp(-time/t1) + A2*exp(-time/t2) + y0

Table S12. Results of two-term exponential fittings of the tenebrescence fading curves.

	Na		K		Rb	
	Value	Standard Error	Value	Standard Error	Value	Standard Error
y0	440.1876	4.10996	124.0854	8.13498	368.0935	5.55667
A1	1466.173	19.97731	1982.931	16.85679	2678.317	17.97594
t1	76.6888	2.11255	96.70841	1.67369	87.65946	1.19231
A2	1933.341	13.9659	2701.185	9.04473	3019.859	11.47398
t2	744.424	9.06995	1152.787	12.66359	917.1071	7.74822
k1	0.01304	3.59E-04	0.01034	1.79E-04	0.01141	1.55E-04
k2	0.00134	1.64E-05	8.67E-04	9.53E-06	0.00109	9.21E-06
tau1	53.15663	1.46431	67.03317	1.16012	60.76091	0.82645
tau2	515.9954	6.28681	799.0512	8.77773	635.6902	5.37065
Reduced Chi-Sqr	5401.724		4920.271		4928.513	
Adj. R-Square	0.98548		0.99331		0.99511	

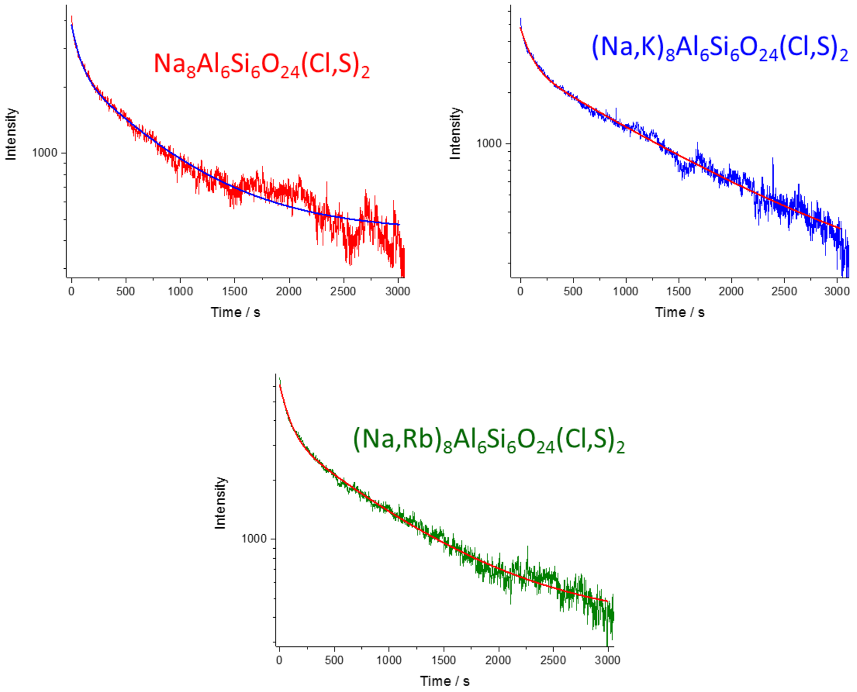

Figure S15. Two-term exponential fittings of the tenebrescence fading curves.

XII. UVI indication without filter and lens

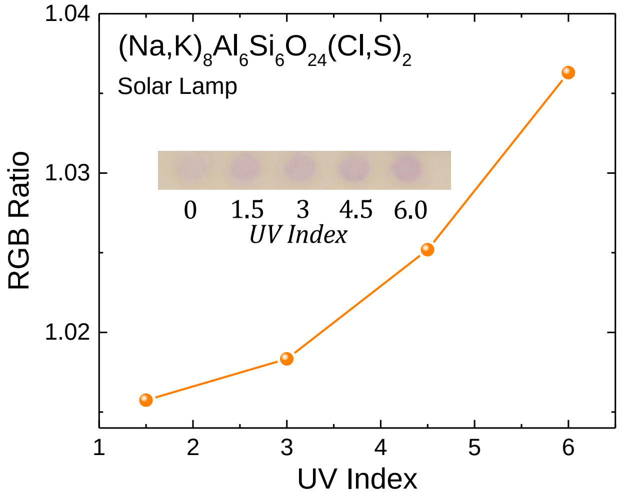

Figure S16. Color intensity of $(Na,K)_8Al_6Si_6O_{24}(Cl,S)_2$ at different UV index values obtained with RGB ratio from the photo shown in the inset. No concentrating lens or vis filter were used.

References

1 H. M. Rietveld, *J. Appl. Cryst.*, 1969, **2**, 65–71.

2 J. Rodríguez-Carvajal, *Phys. B*, 1993, **192**, 55–69.

3 C. A. Schneider, W. S. Rasband and K. W. Eliceiri, *Nat. Methods*, 2012, **9**, 671–675.

4 *IBM SPSS Stat. Wind. Version 23.0. (IBM Corp., Armonk, NY, 2014).*

5 *CasaXPS Process. Softw. XPS, AES, SIMS More (Casa Softw. Ltd., 2016).*

6 C. Adamo and V. Barone, *J. Chem. Phys.*, 1999, **110**, 6158–6170.

7 R. Dovesi, R. Orlando, A. Erba, C. M. Zicovich-Wilson, B. Civalleri, S. Casassa, L. Maschio, M. Ferrabone, M. De La Pierre, P. D’Arco, Y. Noël, M. Causà, M. Rérat and B. Kirtman, *Int. J. Quantum Chem.*, 2014, **114**, 1287–1317.

8 C. R. Dovesi, V. R. Saunders, Roetti, R. Orlando, C. M. Zicovich-Wilson, F. Pascale, B. Civalleri, K. Doll, N. M. Harrison, I. J. Bush, P. D’Arco, M. Llunell, M. Causà and Y. Noël, 2014, CRYSTAL14 User’s Manual (University of Torino).

9 A. Curutchet and T. Le Bahers, *Inorg. Chem.*, 2017, **56**, 414–423.

10 D. Arieli, D. E. W. Vaughan and D. Goldfarb, *J. Am. Chem. Soc.*, 2004, **126**, 5776–5788.

11 W. G. Hodgson, J. S. Brinen and E. F. Williams, *J. Chem. Phys.*, 1967, **47**, 3719.

12 I. Norrbo, J. M. Carvalho, P. Laukkanen, J. Mäkelä, F. Mamedov, M. Peurla, H. Helminen, S. Pihlasalo, H. Härmä, J. Sinkkonen and M. Lastusaari, *Adv. Funct. Mater.*, 2017, 27, 1606547.

13 H. Trill, H. Eckert and V. I. Srdanov, *Phys. Rev. B*, 2005, **71**, 1–6.

14 Y. Takikawa, S. Ebisu and S. Nagata, *J. Phys. Chem. Sol.*, 2010, **71**, 1592–1598.

15 R. Chen and V. Pagonis, *Thermally and Optically Stimulated Luminescence – A Simulation Approach* (Wiley, Wiltshire, UK, 2011).